Supplementary Information

Zeptomolar heavy metal ion detection with density of states sensing

Fangxin Ye [a], Tian Peng [a], Hang Lu [a], Yuying Huang [a], Yu Zhang [a], Yanxi Li *[c], Kuan Zhai [a], Ruiyu Qi [a], Junhong Chen [a], Mengyu Yan *[a, b]

[a]State Key Laboratory of Advanced Technology for Materials Synthesis and Processing, School of Materials Science and Engineering, Wuhan University of Technology, Wuhan, 430070, China
[b]Foshan Xianhu Laboratory, Xianhu Hydrogen Valley, Foshan, 528200, China
[c]School of Microelectronics, Fudan University, Shanghai, 200433, China

*** Corresponding author.**

Email: ymy@whut.edu.cn (Mengyu Yan), liyanxi@fudan.edu.cn (Yanxi Li).

Table of Contents

Supplementary Methods

1. Device fabrication

On-chip monolayer MoS_2 devices were fabricated using standard microfabrication techniques. Monolayer MoS_2 flakes were initially acquired through mechanical exfoliation or chemical vapor deposition (CVD) and subsequently transferred onto an insulating substrate. The as-prepared flakes were pre-selected by optical contrast and further confirmed by atomic force microscopy (AFM), Raman spectroscopy, and photoluminescence (PL) measurements.[1, 2] Metal contact pads (Au-based electrodes) were defined by lithography. Then metal deposition and lift-off procedures were carried out to establish an electrical connection with the MoS_2.[3] An ionic liquid electrolyte, $[BMIM]BF_4$, was employed. A SU-8 polymer layer was then patterned to serve as a passivation layer, electrically isolating the metal interconnects and defining a microscale electrochemical active region. Only the active MoS_2 region is exposed through this window(Fig. 1 and Fig. S1).[4] The SU-8 opening determined the effective MoS_2 area, which was applied for capacitance normalization.

2. Quantum capacitance measurements

Quantum capacitance spectra of monolayer MoS_2 were measured using a commercial CORRTEST electrochemical workstation. Experiments were conducted in a three-electrode configuration, with the instrument operated in single-frequency electrochemical impedance spectroscopy (EIS) mode. In the optical photograph (Fig. S1a), the chip is mounted on the probe station, and the three electrodes are directly wired: the on-chip Au contact connected to the MoS_2 serves as the working electrode (WE), a macroscopic counter electrode (CE) is immersed in the electrolyte droplet, and a reference electrode (RE) is inserted from the top to define the electrochemical potential. The inset highlights the lithographically defined reaction window, where only the exposed MoS_2 is in contact with the electrolyte, while the surrounding metal leads and SiO_2 surface are passivated. The cross-sectional sketch (Fig. S1b) shows the vertical stack: a Si/SiO_2 substrate with Au contacts and monolayer MoS_2, coated with a patterned SU-8 passivation layer and sealed by a PDMS micro-well for electrolyte confinement above the active area.

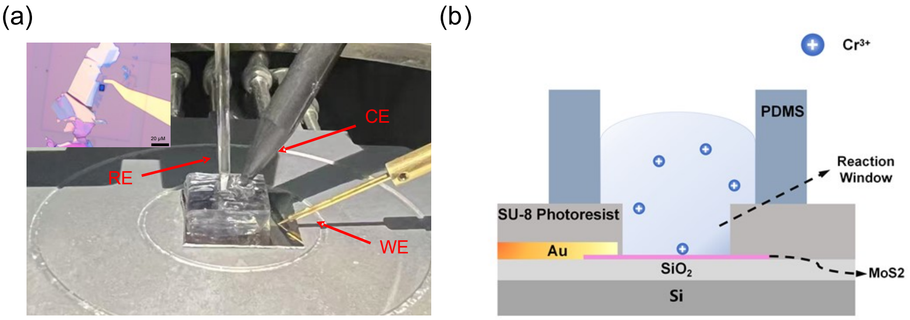

Figure S1. Quantum capacitance measurement setup and microfabricated reaction window. (a) Photograph of the quantum capacitance measurement setup; the inset shows an optical micrograph of the exposed monolayer MoS_2 reaction window. (b) Cross-sectional schematic of the microfabricated reaction window.

Impedance measurements were performed by superimposing a small AC perturbation (50 mV) on a series of DC potentials, applied to the WE versus RE. Different from FET-type measurements, no extra lateral bias was added. Instead, the electronic states of MoS_2 were only modulated by electrochemical potential control in the three-electrode system. At each applied potential, the complex impedance, $Z(f)=Z'(f)+iZ''(f)$ over a broad frequency range. The total interfacial capacitance was extracted from the imaginary part of the impedance as

$$C_T = -\frac{1}{2\pi f Z''}$$

with the frequency (5 Hz) with the response is dominated by capacitive behavior.

The present analysis is focused on the band-gap and low-density-of-states (DOS) energy region of monolayer MoS_2. Within the conventional series-capacitance model,

$$\frac{1}{C_T} = \frac{1}{C_{DL}} + \frac{1}{C_Q}$$

the condition $C_Q \ll C_{DL}$ is expected to hold. Therefore, in the spectral windows used for quantitative evaluation, the total capacitance C_T is approximately equal to the quantum capacitance C_Q in the spectral windows used for quantitative evaluation. Under this approximation

$$C_Q \approx e^2 D(E_F) \quad 5$$

the in-gap peaks and related DOS features in C_Q provide a direct, energy-resolved electrical readout. This readout reflects the adsorption-driven surface DOS evolution. This in-gap–focused strategy forms the basis for the multi-signal quantification of ultratrace Cr^{3+} ions.

To assess possible distortion from parasitic capacitances and non-active regions, the device was designed with a microscale exposed MoS_2 window, while the surrounding region was passivated by SU-8 and the ionic liquid was spatially confined. A comparison between the spectra measured at 5 Hz and 100 Hz is shown in Fig. S2. The 5 Hz spectrum exhibits clear characteristic features, whereas the 100 Hz spectrum is much flatter and the corresponding peaks are strongly suppressed, indicating that the lower frequency is more suitable for resolving the adsorption-induced interfacial capacitance response in this system.

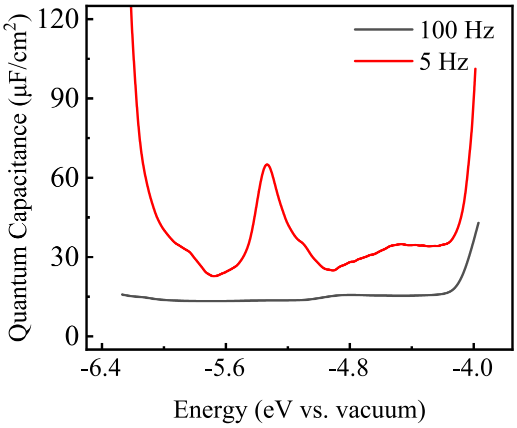

Figure S2. Comparison of the capacitance spectra measured at 5 Hz and 100 Hz.

In addition, a control measurement was performed on a SU-8 passivated region without an exposed MoS_2 window (Fig. S3). No characteristic peak structure is observed in this control spectrum; instead, only low-level noise-like fluctuations are present, with a magnitude at least one order lower than that of the active device. This result indicates that the spectral features discussed in the main text originate primarily from the active MoS_2/electrolyte interface rather than from background parasitic capacitance associated with the passivated regions.

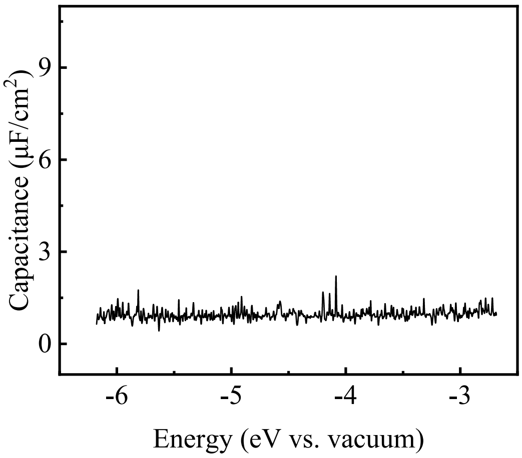

Figure S3. Capacitance spectrum of the SU-8-passivated control region without an exposed MoS_2 window

The horizontal axis of the experimental quantum capacitance spectra was converted. The original axis was the measured electrochemical potential V (vs. Ag/AgCl), and it was changed to an energy scale E (in eV) referenced to the vacuum level. The standard hydrogen electrode (SHE) has a conventional absolute potential of 4.44 eV below vacuum. The Ag/AgCl reference electrode is approximately 0.20 V positive of SHE, the Ag/AgCl electrode lies at around 4.64 eV below vacuum. The electron energy can be written as $E_{vac} \approx -e(V_{vs\ Ag/AgCl} + 4.64)$ where e is elementary charge.[6] This adjustment allow direct comparison with the simulated DOS. They are used to analyze Cr^{3+}-induced effects, including in-gap defect states, apparent band-gap narrowing and band-edge slope changes.

3. Reliability Validation

To evaluate the reproducibility of the adsorption-induced quantum capacitance response, repeated measurement cycles were carried out at representative Cr^{3+} concentrations of 10^{-20}, 10^{-19}, and 10^{-18} M. Owing to the finite lifetime and stability of the device during repeated adsorption and quantum capacitance measurements, extensive repeated cycling was not always feasible. Nevertheless, the overlaid spectra obtained from repeated measurements show good reproducibility in the overall spectral shape and in the positions of the characteristic features (Fig. S4). In addition, statistical analysis of the extracted characteristic peak capacitance values shows only limited variation among repeated measurements (Fig. S5), indicating that the key DOS-related fingerprints and the extracted spectral parameters are reproducible across independent adsorption cycles.

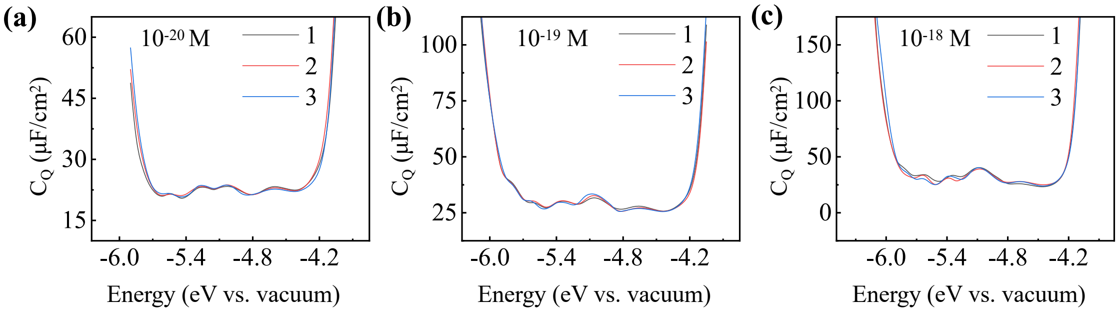

Figure S4. Repeated quantum capacitance spectra measured after independent adsorption cycles at representative Cr^{3+} concentrations of (a) 10^{-20}, (b) 10^{-19}, (c) 10^{-18} M.

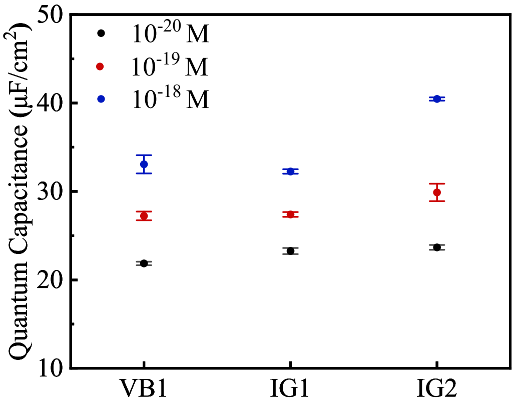

Figure S5. Reproducibility analysis of the extracted characteristic peak capacitance values at representative Cr^{3+} concentrations.

To further distinguish native defect-related features from adsorption-induced spectral evolution, we also measured a defect-containing MoS_2 region without Cr adsorption. The corresponding quantum capacitance spectra show highly reproducible in-gap defect features over three repeated measurements (Fig. S6). This result confirms that native defect-related signatures are stable and identifiable in our platform, which helps us distinguish pre-existing defect responses from the Cr-adsorption-induced spectral evolution discussed in the main text.

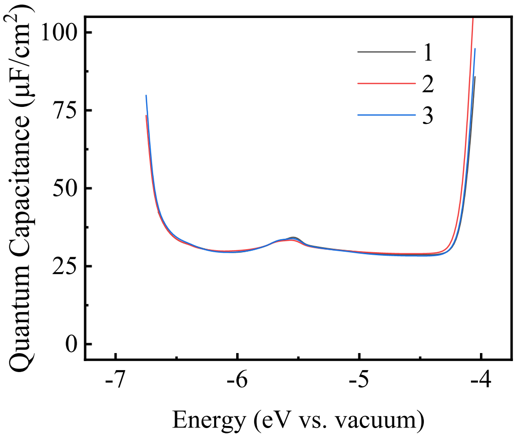

Figure S6. Repeated quantum capacitance spectra measured on a defect-containing MoS_2 region without Cr adsorption.

4. First-principles calculations and quantum capacitance modeling

First-principles calculations were carried out using density functional theory (DFT) within the Vienna Ab initio Simulation Package (VASP). A 3×4 monolayer MoS_2 supercell was employed to model three distinct surface configurations: the pristine basal plane, the surface with adsorbed H_2O, and the surface with Cr^{3+} adsorption. The pristine structure was fully relaxed with no adsorbates present. The DI-water-treated state was modeled by placing a single H_2O molecule on the MoS_2 surface, representing adsorbed water. For Cr^{3+} adsorption, the ion was placed at the hexagon center above the basal plane. This allowed favorable coordination with adjacent top-layer S atoms (Fig. 3).[7]

To model the Cr^{3+} adsorption case, a charged periodic supercell was adopted. Specifically, the total number of electrons was reduced by three ($NELECT=N_{neutral}-3$), so that the supercell carried a formal +3 charge corresponding to the Cr^{3+}-adsorbed configuration. In such charged-cell calculations, VASP automatically introduces a uniform compensating background charge to ensure overall charge neutrality under periodic boundary conditions. Because the present system is a two-dimensional monolayer slab, dipole correction was applied along the out-of-plane direction using LDIPOL=.TRUE.. and IDIPOL=3. In addition, LCORR=.TRUE. was used to reduce the electrostatic error associated with the charged supercell, improving the reliability of the calculated energetics and electronic structure for the 2D charged system.

The projector-augmented-wave (PAW) method was used to describe the core–valence interaction,[8] and the exchange–correlation functional was treated within the generalized gradient approximation using the Perdew–Burke–Ernzerhof (PBE) form. A plane-wave cutoff energy of 520 eV and a 3 × 3 × 1 Monkhorst–Pack k-point mesh were adopted after convergence tests. A vacuum spacing of at least 10 Å was introduced along the out-of-plane direction to minimize interactions between periodic images. All atomic structures were relaxed until the residual forces on each atom were below 0.02 eV $Å^{-1}$ (or tighter). Spin polarization was included for configurations involving Cr^{3+}.

For the relaxed configurations (pristine, H_2O-adsorbed, and Cr^{3+}-adsorbed MoS_2), the band structures, total density of states (DOS), and element-/orbital-projected DOS (S 3p, Mo 4d, and Cr 3d) were calculated. Charge redistribution induced by Cr^{3+} adsorption was visualized using the charge-density difference defined as

$$\Delta\rho_{(r)} = \rho_{MoS_2+Cr^{3+}}(r) - \rho_{MoS_2}(r) - \rho_{Cr^{3+}}(r)$$

Theoretical quantum capacitance spectra can be derived from the calculated DOS as

$$C_Q(E) = e^2 \int D(E')\left(-\frac{\partial f(E' - E_F)}{\partial E'}\right)dE'$$

where D(E′) is the total DOS, f is the Fermi–Dirac distribution at 300 K, and E denotes the electrochemically tuned energy referenced to the Fermi level in the supercell.

5. Raman and PL Characterization

In the Raman spectra (Fig. S7a), the in-plane E^{1}_{2g}(~384.9 cm^{-1}) and out-of-plane A_{1g}(~404.1 cm^{-1}) modes remain at characteristic positions of monolayer MoS_2 with narrow linewidths over the entire Cr^{3+} concentration range, indicating that the 2H crystal structure is preserved without detectable phase transformation or severe degradation. As the Cr^{3+} concentration increases, both modes exhibit a slight blue shift together with subtle linewidth variations, consistent with modest lattice stiffening induced by local strain and/or charge transfer while remaining in a weak-distortion regime. The PL spectra provide complementary information on recombination dynamics (Fig. S7b).[9] Pristine monolayer MoS_2 shows a pronounced excitonic emission peak at 1.84 eV,[10] which undergoes progressive quenching and a small redshift upon exposure to increasing Cr^{3+} concentrations. These trends point to the emergence of additional non-radiative recombination channels and the formation of localized states at or near the band edges, which shorten the exciton lifetime and renormalize the effective band-edge energies.[11, 12] The Raman and PL results show that Cr^{3+} adsorption leaves the monolayer lattice intact but introduces new electronic states close to the band edges.

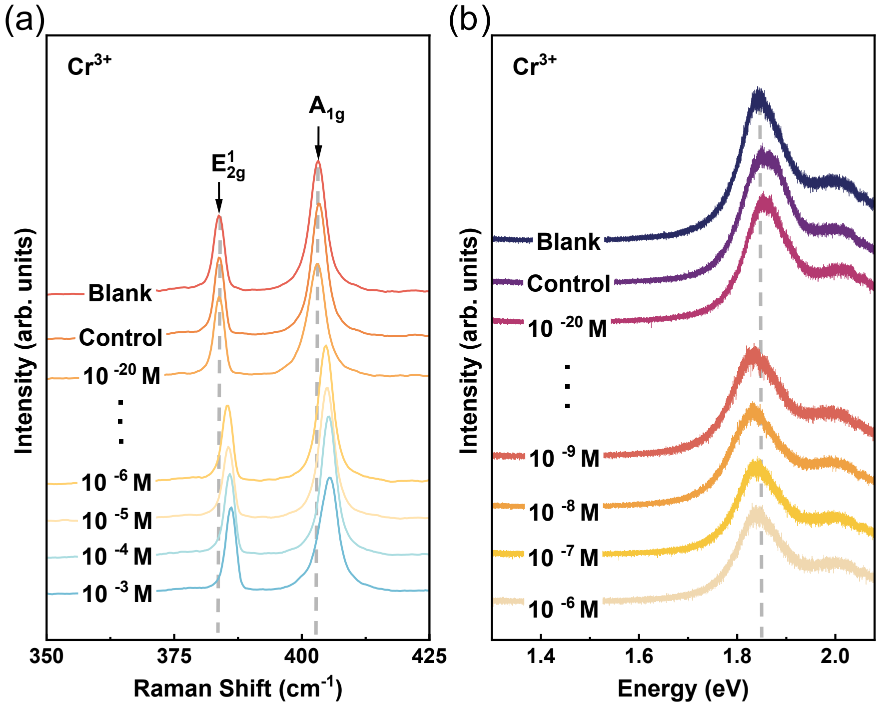

Figure S7. Raman and PL spectroscopy characterization of monolayer MoS_2 after Cr^{3+} ion adsorption. (a) Raman, (b) PL.

6. Real-space visualization of Cr^{3+}-induced charge redistribution

Figure S8 provides orthogonal views of the charge–density difference associated with Cr^{3+} adsorption on monolayer MoS_2. The three-dimensional isosurface (Fig. 3c) shows that the redistribution is highly localized around the adsorbed ion and the three nearest S atoms in the top chalcogen layer, while the lower S layer remains almost unaffected. The top view (Fig. S8a) highlights the approximately C_3-symmetric "lobes" of charge accumulation (yellow) centered on the hexagon center site above the Mo–S hexagon, surrounded by a ring-like depletion (cyan) on neighboring Mo sites, indicating a directional Cr–S coordination and net electron transfer from the MoS_2 host toward the adsorbate. The side view (Fig. S8b) further reveals that the accumulation extends mainly into the electrolyte side, consistent with partial occupation of Cr-centered states and polarization of the top S layer. These results confirm that Cr^{3+} perturbs the electronic structure in a strongly localized manner at the interface.

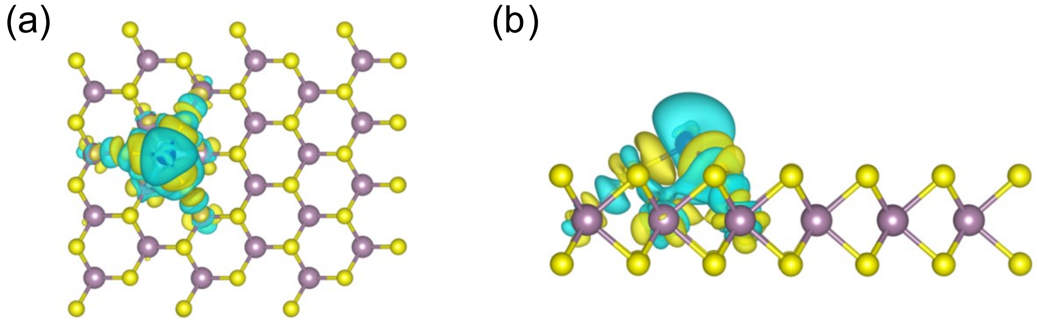

Figure S8. Charge–density difference maps for Cr^{3+} adsorbed on monolayer MoS_2. (a) top view, and (b) side view of $\Delta\rho_{(r)} = \rho_{MoS_2 + Cr^{3+}}(r) - \rho_{MoS_2}(r) - \rho_{Cr^{3+}}(r)$. Cyan and yellow isosurfaces denote charge depletion and accumulation, respectively.

7. Projected DOS analysis

Complementing the band-structure results presented in Fig. 8, Fig. S9 displays the total and projected DOS of monolayer MoS_2 prior to and following Cr^{3+} adsorption. The absence of significant in-gap states in the reference configuration indicates a relatively defect-free basal plane within the supercell model (Figs. S9a–c).

After Cr^{3+} adsorption (Figs. S9d–g), new DOS features appear within the band gap and near the conduction band edge. The in-gap region shows substantial weight on Cr-3d states that is strongly hybridized with neighboring S-3p orbitals, while the nearby Mo-4d DOS is slightly redistributed but remains largely band-like. At higher energies, the enhanced DOS close to the conduction edge is still dominated by Mo-4d states, with a non-negligible Cr-3d admixture that reflects the formation of Cr–S–Mo coordination states rather than isolated impurity levels.

This orbital-resolved picture confirms that the new gap states and the strengthened conduction-band DOS originate from localized Cr-centered coordination complexes embedded in the MoS_2 host. Because quantum capacitance is directly proportional to DOS, the narrow Cr-derived features in the gap and at the band edge naturally give rise to the distinct energy-resolved peaks and slope changes observed in the experimental C_Q spectra, without invoking structural degradation of the monolayer.

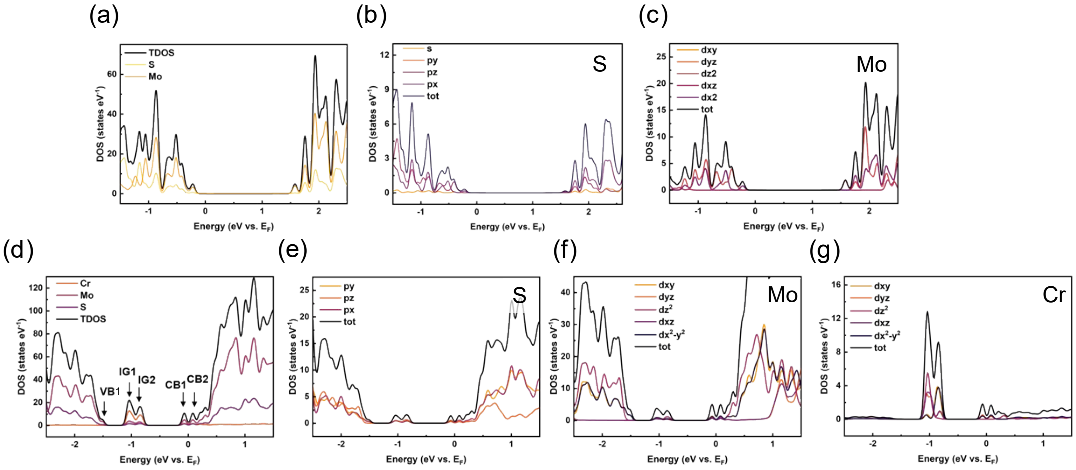

Figure S9. Calculated density of states (DOS) of monolayer MoS_2 before and after Cr^{3+} adsorption. (a–c) Total DOS and projected DOS of intrinsic MoS_2: (a) total, (b) S, and (c) Mo contributions. (d–g) DOS after Cr^{3+} adsorption: (d) total, (e) S-projected, (f) Mo-projected, and (g) Cr-projected DOS.

8. Extension to other adsorbed ion

To illustrate the generality of the DOS-based sensing concept, we also carried out calculations for other transition-metal ions adsorbed on monolayer MoS_2. Figure S10 shows the total DOS for MoS_2 with Ti and V adsorbed at the same hexagon center site as used for Cr , with all computational parameters held constant.

For Ti adsorption, new electronic states emerge near the Fermi level, and the conduction band edge exhibits increased structural complexity (Fig. S10a). In the case of V adsorption, states appear within the band gap and in proximity to both the valence and conduction band edges (Fig. S11b).The DOS profile differs clearly from that of pristine MoS_2 and from the Cr^{3+}-adsorbed case.

These results confirm that ion adsorption in general can reshape the band-edge and in-gap DOS of monolayer MoS_2. In principle, the distinct DOS patterns could be read out by quantum capacitance measurements and used as fingerprints for different ions. A systematic exploration of multi-ion sensing and selectivity is beyond the scope of this work and will be addressed in future studies.

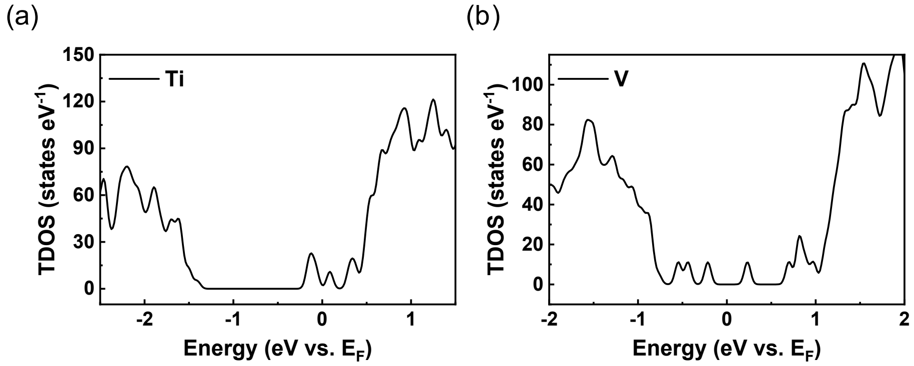

Figure S10. DFT-calculated total density of states (TDOS) of monolayer MoS_2 after adsorption of different transition-metal ions. (a) TDOS of Ti-adsorbed MoS_2 referenced to the Fermi level E_F. (b) TDOS of V-adsorbed MoS_2.

9. Comparison of quantum capacitance and current responses

Figure S11 compares the concentration dependence of quantum capacitance and current at several Cr^{3+}-induced DOS fingerprints. C_Q at VB1, IG2 and CB1 (Figs. S11a–c) increases monotonically as the Cr^{3+} concentration rises from 10^{-20} to 10^{-15} M. Linear fits versus log C give R^2 values of about 0.81 for VB1, 0.95 for IG2 and 0.93 for CB1, showing that these DOS features provide stable and linear calibration curves over five orders of magnitude in concentration, with CB1 and IG2 demonstrating the highest robustness.

The corresponding current (I) at IG1, IG2, VB1 and CB1 is showing in Fig. S11d. I at VB1 grows with concentration, but the responses at IG1, IG2 and CB1 are much weaker and show larger scatter, with an average R^2 of 0.81. In this ultratrace concentration regime, the current signal is more susceptible to background contributions, including residual faradaic processes on the electrodes and parasitic conduction through the electrolyte and wiring.[13, 14] These background currents do not follow the local DOS change at a fixed energy and therefore reduce the linearity and reliability of the changes I with the logarithm of ion concentrations calibration, especially for localized in-gap states. These results confirm that DOS-resolved quantum capacitance readout provides a more robust and more linear access to Cr^{3+}-induced electronic fingerprints than conventional current sensing, for in-gap and band-edge features.

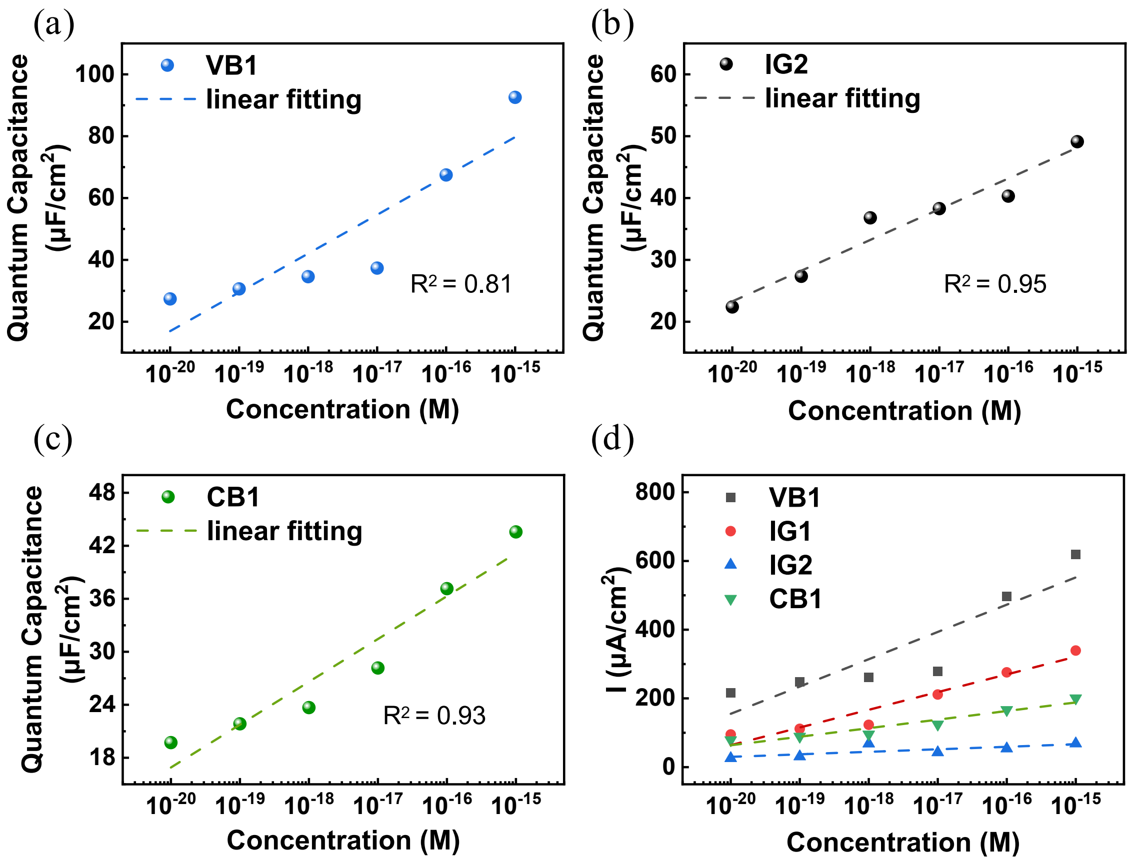

Figure S11. Comparison of quantum capacitance and current responses. (a-c) Concentration-dependent C_Q at VB1 (a), IG2 (b), and CB1 (c). (d) Corresponding current I at IG1, IG2, VB1 and CB1.

10. Comparison of representative MoS_2-based sensors for heavy-metal ion detection

To contextualize the current study, Table 1 summarizes representative MoS_2-based sensors for heavy-metal ion detection, including the target ions, materials or structures, and limits of detection (LOD). As shown, most studies employ traditional electrochemical sensing methods, with LODs ranging from femtomolar to micromolar concentrations. In contrast, our approach utilizes a DOS-sensing platform based on the quantum capacitance of MoS_2, achieving an ultralow detection limit of 10 zM for Cr(III) by directly probing the electronic fingerprints induced by ion adsorption.

Table 1 Comparison of MoS_2-based sensors for heavy-metal ion detection

Metal Ions	Materials or structures	LOD	Reference
Hg(II)	solvent exfoliated of MoS_2-coated glassy carbon electrode	1 fM	13
Pb(II)	Sensor Based on Biomass Yeast Integrated Sulfur-doped Graphene and Carboxylated Carbon Nanotubes/MoS_2	0.0126 fM	14
Cd(II)	PEI-MoS_2@Au NPs 3D flower-like nanocomposites	0.234 fM	15
Cu(II)	Polyaniline Functionalization of Defective 1T-MoS_2 Nanosheets	0.33 nM	16
As(III)	Fe_3O_4/MoS_2 nanocomposite	0.28 nM	17
Ag(I)	MoS_2-based field effect transistor	0.1 nM	18
Cr(III)	Fe_3O_4 nanospheres on MoS_2 nanoflake	0.5 µM	19
Cu(II)	MoS_2 Modified Screen Printed Carbon Electrode Based Flexible Electrochemical Sensor	5.43 µM	20
Mn(II)	MoS_2-biopolymer-coated screen-printed carbon electrode	0.187 nM	21
Cr(III)	**DOS sensor**	**10 zM**	**This Work**

Supplementary References

1. K. S. Novoselov, A. K. Geim, S. V. Morozov, D. Jiang, Y. Zhang, S. V. Dubonos, I. V. Grigorieva and A. A. Firsov, *Science*, 2004, **306**, 666–669.
2. Q. H. Wang, K. Kalantar-Zadeh, A. Kis, J. N. Coleman and M. S. Strano, *Nature Nanotechnology*, 2012, **7**, 699–712.
3. J. Xia, F. Chen, J. Li and N. Tao, *Nature Nanotechnology*, 2009, **4**, 505–509.
4. Z. Zhang, P. Zhao, G. Xiao, B. R. Watts and C. Xu, *Biomicrofluidics*, 2011, **5**, 46503–465038.
5. S. Luryi, *Applied Physics Letters*, 1988, **52**, 501–503.
6. *Journal of Electroanalytical Chemistry and Interfacial Electrochemistry*, 1986, **209**, 417–428.
7. H. Liu, W. C. Silva, L. Santana Gonçalves de Souza, A. G. Veiga, L. Seixas, K. Fujisawa, E. Kahn, T. Zhang, F. Zhang, Z. Yu, K. Thompson, Y. Lei, C. J. S. de Matos, M. L. M. Rocco, M. Terrones and D. Grasseschi, *Nanoscale*, 2022, **14**, 10801–10815.
8. G. Kresse and D. Joubert, *Physical Review B*, 1999, **59**, 1758–1775.
9. M. G and O. M, *Физик сэтгүүл*, 2022, **20**, 85–89.
10. A. Splendiani, L. Sun, Y. Zhang, T. Li, J. Kim, C.-Y. Chim, G. Galli and F. Wang, *Nano Letters*, 2010, **10**, 1271–1275.
11. P. K. Chow, R. B. Jacobs-Gedrim, J. Gao, T.-M. Lu, B. Yu, H. Terrones and N. Koratkar, *ACS Nano*, 2015, **9**, 1520–1527.
12. Z. Li, H. Bretscher, Y. Zhang, G. Delport, J. Xiao, A. Lee, S. D. Stranks and A. Rao, *Nature Communications*, 2021, **12**, 6044.
13. R. Aswathi and K. Y. Sandhya, *Journal of Materials Chemistry A*, 2018, **6**, 14602–14613.
14. M. Yin, H. Pu, Y. Zhang, P. Gao, Q. Sun, W. Yin and H. Fa, *Electroanalysis*, 2023, **35**, e202200163.
15. M. Li, B. He, H. Yan, L. Xie, X. Cao, H. Jin, M. Wei, W. Ren, Z. Suo and Y. Xu, *Analytica Chimica Acta*, 2022, **1232**, 340470.
16. X. Gan, J. Zhang, J. Liu, Y. Bai, X. Su, W. Wang, Z. Cao, H. Zhao, Y. Ao and P. Wang, *ACS Applied Nano Materials*, 2023, **6**, 11725–11736.
17. X.-B. Xia, X. Cheng, Z. Liu, J. Y. Li and S. Li, *Sensors and Actuators B: Chemical*, 2022.
18. C. Kou, H. Hu, Y. Tang, Y. Luo, C. Han, Y. Bao, Z. Guo and L. Niu, *Talanta*, 2025, **283**, 127141.
19. A. Garcia-Miranda Ferrari, R. D. Crapnell, P. S. Adarakatti, B. P. Suma and C. E. Banks, *Sensors and Actuators Reports*, 2022, **4**, 100116.
20. D. Neethipathi, A. Beniwal, A. Bass, E. M. Scott and R. Dahiya, *IEEE Sensors Journal*, 2023, **PP**, 1–1.
21. J. Wang, Z. Wang, Y. Cheng, L. Cao, F. Bai, S. Yue, P. Xie and J. Ma, *Water Research*, 2021, **201**, 117291.